ELSEVIER

Journal of Nuclear Materials 300 (2002) 7–14

journal of nuclear materials

www.elsevier.com/locate/jnucmat

The dissolution of oxide on α-Zr(1%Nb) and β-Zr(20%Nb) alloys

Chunsi Zhang, Peter R. Norton *

Interface Science Western, Department of Chemistry, The University of Western Ontario, Chemistry Building, London, Ontario, Canada N6A 5B7

Received 5 May 2001; accepted 4 October 2001

Abstract

The oxide dissolution rates on β-Zr(20%Nb) and α-Zr(1%Nb) alloys have been measured by AES at various temperatures. The results indicated that oxide films on the β-Zr(20%Nb) alloy dissolve much more rapidly into the bulk alloy than is the case for the α-Zr(1%Nb) alloy. The oxygen diffusion coefficients in both the β-Zr(20%Nb) and α-Zr(1%Nb) alloys were deduced from the oxide dissolution kinetics, which are $0.172\exp(-187.47$ kJ/RT) and $0.69\exp(-149.45$ kJ/RT) for the α-Zr(1%Nb) alloy and β-Zr(20%Nb) alloy, respectively.

1. Introduction

Because of their low neutron absorption cross-section and high strength at high temperatures, zirconium (Zr) alloys have been widely used for components in nuclear reactors. Delayed hydride cracking is a major cause of failure of components made from Zr in service. During production, Zr–Nb pressure tubes (PT) are stress relieved at 673 K in steam; this also results in the formation of a dense oxide layer ≈1-μm thick which is an effective barrier against deuterium ingress. During reactor operation at ~673 K this oxide film grows, increasing in thickness during the lifetime to ~10s of μm. Accompanying this oxide growth in D_2O is the release of D, a fraction of which finds its way into the underlying PT. The growth of the oxide is complicated, depending on the morphology, microstructure and chemistry at the alloy–oxide interface. At 673 K, the competing process of oxide dissolution is also occurring, and is one of the factors that must be considered in evaluating that stability of the oxide film and its role in determining the lifetime of components fabricated from Zr alloys [1–3]. [1] Differences in dissolution rates between the various phases in the alloy may therefore play a significant role in determining the properties and kinetics of *net* oxide growth at the interface.

A number of papers have reported the rate of dissolution of Zr oxide on Zr or Zr alloys [1,4], including data for Zr–2.5%Nb alloy, the most commonly used Zr alloy in the Canadian nuclear industry. The microstructure of Zr–2.5%Nb alloy is composed of two phases: α-Zr (hexagonally close packed, containing $\leqslant 1$%Nb), and β-Zr (body-centered cubic, containing $\geqslant 20$%Nb). It has been reported that there is a difference in the oxide dissolution rates on these two phases, but to the authors' knowledge, no *quantitative* results have been reported in the literature. Transmission electron microscopy and scanning electron microscopy were used to study an oxide film on the surface of a Zr–2.5%Nb PT which had failed after a long period of service in-reactor. It was found that the interface

* Corresponding author. Fax: +1-519 661 3022.
E-mail address: pnorton@uwo.ca (P.R. Norton).

[1] These are proprietary reports. The intent is that the reader can identify the source and if necessary seek clearance from the Candu Owners Group for access.

0022-3115/02/$ - see front matter
PII: S0022-3115(01)00714-0

between the oxide film and the bulk metallic alloy and the oxide near to the interface, had significantly changed in service [5]. A very complicated structure containing holes, ridges, cracks etc., was observed in the oxide and at the interface. Some of these features appeared to be related to the presence of the two alloy phases in the bulk alloy at the inference. An interface was thereby drawn that the formation of these very complicated structures must, at least partially, correspond to differences in the oxidation and oxide dissolution kinetics on/in these two phases. We present in this paper the results of a quantitative study that will provide a better understanding of the stability of oxide films on Zr–2.5%Nb alloys.

2. Experimental section

The experiments were carried out in a two-level ultrahigh-vacuum chamber equipped with a number of surface analytical techniques, including Auger electron spectroscopy (AES) and nuclear reaction analysis (NRA). The general experimental arrangement has been described previously [6]. The base pressure in the chamber (5×10^{-11} Torr) was achieved by using liquid nitrogen trapped diffusion and Ti-sublimation pumps.

The samples (nominally α-Zr(1%Nb) alloy and β-Zr(20%Nb) alloy) were provided by Chalk River Laboratories (CRL) of AECL. The compositions of these two alloys, including the impurities, are listed in Table 1. The samples were cut into $\approx 5 \times 5 \times 1$ mm^3 samples and then polished by fine sand paper (400 A grade). They were then spot welded to two platinum wires which acted as sample supports, heaters and thermal conductors for cooling. The ends of these platinum wires were spot welded to two Ni-plated copper posts welded to a UHV manipulator filled with liquid nitrogen. The sample could thereby be resistively heated by passage of a current through the Pt wires, and also cooled via the copper posts and the same platinum wires. A programmable temperature controller allowed for linear temperature ramps as well as isothermal experiments. The temperature was measured by a Ni–Cr/Ni–Al thermocouple spot welded to the edge of the samples. The sample temperature could be controlled with a precision of better than ±0.5 K. The as-received samples, after being mounted in the chamber, were sputtered by a 3 keV Ar^+ ion beam of current density 1 μA/cm^2, to remove the oxide and other contaminants on the surface. Before each experiment, the α-Zr(1%Nb) alloy sample was heated to 873 K and held at that temperature for a few minutes to dissolve the contaminants that had accumulated on the surface since the previous experiment. The β-Zr(20%Nb) alloy was heated to 1093 K and held for a few minutes before each experiment; this not only resulted in the dissolution of the surface contaminants, but also the formation of a single β-phase. After the 1093 K heating, the β-Zr(20%Nb) alloy sample was quenched to low temperatures at a rate of about 50–100 K/s; this maintained the β-phase microstructure without transformation [7]. After the heating and quenching treatments, Fe and H segregated to the surfaces of the α-Zr(1%Nb) alloy and the β-Zr(20%Nb) alloy, respectively. A brief Ar^+ sputtering treatment was carried out before each experiment to remove these segregants.

The surface composition was measured by AES using a computer controlled single pass cylindrical mirror analyzer with a modulation voltage of 1 V. It has been noted previously [8] that Zr oxide might be damaged by a high current density electron beam. In order to reduce this potential damage during the AES experiments, the 3 keV, 0.1 μA electron beam was rastered over a 0.2×0.2 mm^2 area, which resulted in an electron beam density of 2.5 μA/mm^2. We have shown that no changes are detectable in the oxide AES spectra under these conditions [8]. The magnetic field resulting from the passage of the heating current through the platinum support wires affects the intensities of different Auger electrons by different amounts. Separate experiments were carried out to measure the effect of the heating current on the intensities of the Auger transitions used in these measurements, and all experimental data then were corrected for these effects.

Absolute oxygen coverages were measured using the $^{18}O(p, \alpha)^{15}N$ reaction by using 750 keV H^+. The number of particles emitted was referenced to the yield from a Ta_2O_5 target of known oxygen coverage in the same geometry. This method is capable of an absolute accuracy of 3–5% [9]. The dosing was carried out using $^{18}O_2$. The use of the ^{18}O reaction eliminated the problem of the ^{16}O background in the sample.

The measurements were carried out in the following way. An oxide film was first grown on the alloy surfaces at ~90 K. The uniformity and thickness of a representative oxide film grown at this temperature was determined by AES as described below. If the film met the

Table 1
Compositions of α-Zr(1%Nb) alloy and β-Zr(20%Nb) alloy (in w/w; ppmw)

	Nb (%)	C (ppm)	Cu (ppm)	Fe (ppm)	Hf (ppm)	O (%)
α-Zr(1%Nb) alloy	0.99	45	60	495	46	0.107–0.108
β-Zr(20%Nb) alloy	19.9	186	90	630	95	0.135–0.194

necessary criteria for uniformity and thickness, the sample was carefully positioned in front of the CMA and the temperature was then either ramped continuously at a chosen rate to a maximum temperature, with continuous monitoring of the AES transitions, or it was ramped to one of a set of chosen fixed temperatures for isothermal measurements. The computer-controlled CMA permitted repetitive peak jumping between prechosen electron kinetic energies which could be used to evaluate the peak-to-peak intensities of the relevant Auger transitions and hence their time and temperature dependence.

3. Results and discussions

3.1. The oxides on the surfaces of α-Zr(1%Nb) and β-Zr(20%Nb) alloys

The quantitative measurement by *surface techniques*, of the amount of oxide on the surface requires that the oxide film on the surface satisfies the following conditions:

1. The thickness of oxide should lie in the range of the sampling depth of the chosen surface technique, which is about 2 nm in the case of AES.
2. The oxide film must be laterally uniform in thickness, because the formula used to calculate the amount of oxide film is only valid for this condition.

We therefore first demonstrate that it is possible to produce oxide films on the alloys that satisfy these criteria. Briefly, the thickness of oxide is determined by AES and NRA measurements and the growth mode of the oxide films and their lateral uniformity in thickness is identified by methods developed in this lab, which use the sum of the AES intensities of oxide and metal. For layer-by-layer growth of an oxide which is laterally uniform in thickness, the sum of the intensities first decreases followed by an increase. In contrast, island growth and the resulting laterally non-uniform thickness of the oxide film, exhibits a constant value for this sum. The details of the methods and analysis of the data on the oxidation of pure α-Zr are available in our previous paper which demonstrates that different growth mechanisms occur at different temperature ranges, and which fit the simple model [10]. In this previous study of the growth of thin oxide films on pure α-Zr at low temperature (90 K), it was found that the oxide grows layer-by-layer, forming a film which is of laterally uniform thickness. The oxide grows linearly with exposure over the first few Langmuir at 90 K (1 Langmuir = 1 L = 1×10^{-6} Torr s), and then passivates at exposures above 15 L. AES and NRA, indicate that the passive oxide film is about 1.5-nm thick, which is within the sampling depth of AES. We have successfully investigated the kinetics of oxide dissolution on α-Zr by using the oxide film formed at low temperature. We have also tried to make use of oxide films grown at higher temperatures, but it was found that the oxide film grows by a mixture of island and layer-by-layer modes, and that the non-uniform thickness of the passive oxide is larger than the sampling depth of AES.

Figs. 1 and 2 show the Auger electron spectra of the surfaces of the α-Zr(1%Nb) alloy and the β-Zr(20%Nb) alloy before and after oxidation at ~100 K respectively. It is seen in these figures that the valence band related Auger transitions from oxidized Zr atoms can easily be

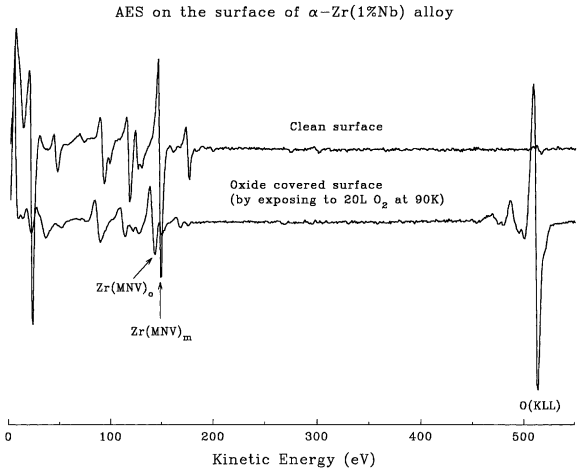

Fig. 1. Auger electron spectra of (a) clean α-(Zr–1%Nb) alloy and (b) the same surface with a 1.5-nm oxide film. The oxide was formed by exposing the Zr alloy to 20 L oxygen at 103 K.

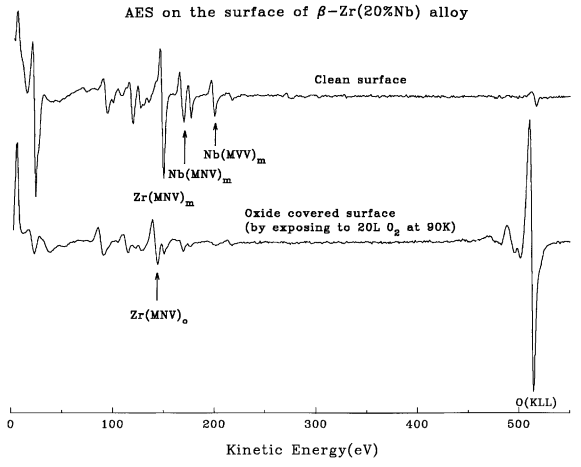

Fig. 2. Auger electron spectra of (a) clean β-(Zr–20%Nb) alloy and (b) the same surface with a 1.5-nm oxide film. The oxide was formed by exposing the Zr alloy to 20 L oxygen at 103 K.

distinguished from those originating from the metallic or non-oxidized Zr atoms, since the valence band structure of Zr is significantly modified by oxidation. As in our previous work, we have used the $Zr(MNV)_m$ Auger transition at 147 eV to determine metallic or non-oxidized Zr, and the $Zr(MNV)_o$ transition at 142 eV for oxidized Zr atoms. However, the $Zr(MNV)_m$ Auger transition in our dissolution experiments occurs in the non-oxidized alloy right below the oxide where dissolved oxygen is saturated. Since dissolved oxygen will change the chemical environment around the Zr atoms and therefore the intensity of $Zr(MNV)_m$ Auger transition [10], the Auger sensitivity factor for the $Zr(MNV)_m$ transition must be determined on the sample surface where the oxygen is saturated but no oxide has been formed. This surface condition was readily achieved by slowly heating a sample initially covered by oxide up to a temperature where the oxide film dissolved into the bulk, followed by cooling. This left a surface containing only a saturated level of dissolved oxygen. Similarly, the Auger sensitivity factor for the $Zr(MNV)_o$ transition was determined in situ on a sample surface covered by an oxide film thicker than the AES sampling depth. This surface was produced by oxidation at higher oxygen partial pressures and higher temperatures.

Based upon this previous experience, we therefore exclusively used oxide films grown on the alloys at low T for the dissolution experiments, after first demonstrating that they also satisfied the criteria listed above. By using the methods developed in our previous work and mentioned above [10] it was found that the growth mode of the oxide film on the surface of the α-Zr(1%Nb) alloy at ~100 K is layer-by-layer with a linear dependence upon exposure over the first few L, followed by passivation. The passive oxide film on the α-Zr(1%Nb) alloy was laterally uniform in thickness, and was measured by AES and NRA to be 1.5-nm thick. The oxidation behaviour and the passive oxide thickness on the surface of the α-Zr(1%Nb) alloy are therefore very similar to those observed on pure α-Zr in our previous work [10], suggesting that the 1%Nb in the α-Zr(1%Nb) alloy has little effect on oxide growth. The oxide thickness, as in previous work, was obtained from either the intensity of the $Zr(MNV)_o$ transition, or the intensity of the $Zr(MNV)_m$ transition by using a well known exponential attenuation formula of Auger electrons used in our previous work [7,9]. It was found that the results from these two Auger transitions agreed closely. In order to improve the statistics, the thickness of the oxide film was taken as the average of those calculated from intensities of the $Zr(MNV)_o$ and $Zr(MNV)_m$ transitions:

$$d = 0.5\lambda(\cos\theta)[\ln(1 - I_o/I_o^0) + \ln(I_m/I_m^0)], \quad (1)$$

where d is the thickness of the oxide, λ is the mean free path of the $Zr(MNV)_o$ and $Zr(MNV)_m$ Auger electrons, which has taken as 0.68 nm from the universal electron attenuation curve [11], θ is the take-off angle, I_o and I_m are the intensities of the $Zr(MNV)_o$ and $Zr(MNV)_m$ transitions, and I_o^0 and I_m^0 are their Auger sensitivity factors, respectively. We have assumed the Zr oxide was composed entirely of ZrO_2. This assumption might not be quite true, because there would be a small amount of sub-oxide at the oxide–metal interface [12]. However, this same assumption was made in our previous work [8], and was found to yield good agreement between our oxygen diffusion results based on this assumption and those in the literature. The number of oxygen atoms in the oxide per unit surface area ($= 2x$ number of oxidized Zr atoms) was obtained from the thickness of oxide and the molecular density of the oxide (2.88×10^{22} molecules/cm^3).

Fig. 2 illustrates the Auger electron spectra of the β-alloy before and after oxidation. It is seen that the $Zr(MNV)_m$ peak is attenuated and the $Zr(MNV)_o$ peak at 142 eV appears upon exposure to oxygen at ~100 K, indicating that Zr atoms are oxidized. Significant attenuation of the $Nb(MNV)_m$ transition (at 167 eV) is also observed, but in contrast to the observation for Zr, no Nb transition attributable to oxidized Nb appeared ($Nb(MNV)_o$ would be located at 162 eV). This indicates that Nb atoms are not oxidized at the surface of the β-Zr(20%Nb) alloy. However, the intensities of the Nb transitions *decrease* with oxygen exposure, due, we believe, to their attenuation by the growing Zr oxide film covering the alloy. This very significant difference in oxidation behavior between Zr and Nb atoms, arises from the difference in their reactivities towards oxygen. A complementary experiment in which pure Nb was exposed to oxygen under the same experimental conditions, also showed that no oxidation occurred. This is entirely consistent with the observation of strong preferential oxidation of Zr in the β-Zr(20%Nb) alloy. Using the same methods employed for the study of the α-Zr(1%Nb) alloy, it was found that at 100 K the Zr oxide film first grew layer-by-layer and then became passive at a thickness of 1.5-nm. The thickness of Zr oxide on the surface is also essentially uniform. Therefore, Eq. (1) is also valid for calculating the thickness of the Zr oxide film on the β-Zr(20%Nb) alloy.

3.2. The oxide dissolution rates on α-Zr(1%Nb) alloy and β-Zr(20%Nb) alloy

Fig. 3 shows the disappearance of oxide from the surfaces of the α-Zr(1%Nb) and β-Zr(20%Nb) alloys during heating at a rate of 1 K/s. It can be clearly seen in Fig. 3 that the oxide on the surface of the β-Zr(20%Nb) alloy dissolves at much lower temperatures than on the surface of the α-Zr(1%Nb) alloy. The oxide starts to dissolve into the β-Zr(20%Nb) alloy at 388 K, compared

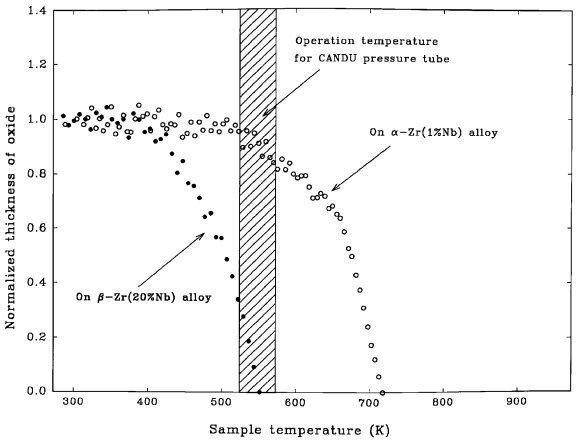

Fig. 3. The change of thickness of Zr oxide films on the surfaces of α-(Zr–1%Nb) alloy and β-(Zr–20%Nb) alloy during linear heating at a rate of 1 K/s.

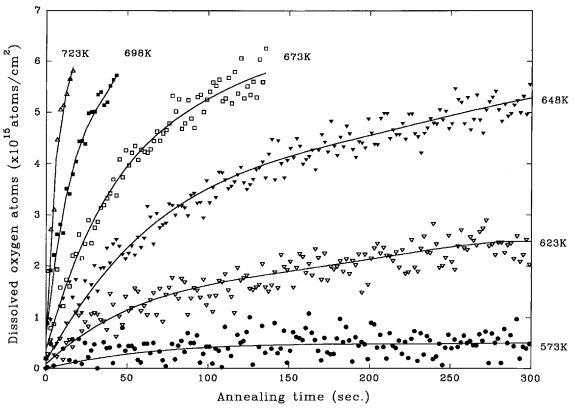

Fig. 4. The change in the amount of dissolved oxygen with time for the α-(Zr–1%Nb) alloy at various temperatures.

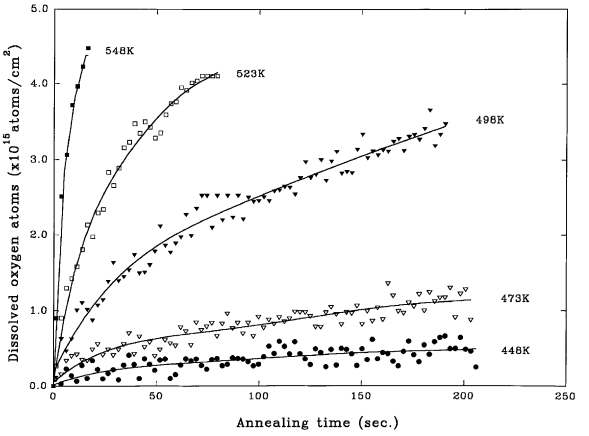

Fig. 5. The change in the amount of dissolved oxygen with time for the β-(Zr–20%Nb) alloy at various temperatures.

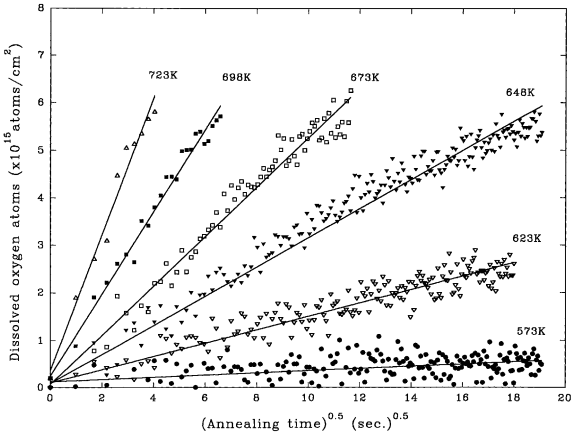

Fig. 6. The linear relationship between the amount of oxygen dissolved from the oxide film into the bulk α-(Zr–1%Nb) alloy and (annealing time)$^{1/2}$ at various temperatures.

to 553 K observed for the α-Zr(1%Nb) alloy. The 1.5-nm thick oxide film had completely dissolved by ~553 K on the β-phase and from the α-alloy surface by 718 K, a difference of 165 K. Note that the oxide on the surface of the β-Zr(20%Nb) alloy rapidly dissolves into the bulk at a temperature below that characteristic of the operation of a Candu (Canada Deuterium Uranium) reactor (~573 K), in which Zr–2.5%Nb alloy PTs are used. Thus it would appear that regrowth of oxide on the β-phase in Zr–2.5%Nb alloy PTs would have to be more rapid than on the α-phase, to maintain the thickness and (presumably) the integrity of the oxide film. This would lead to anticipated differences in morphology and microstructure of the oxide on the β-phase.

Figs. 4 and 5 show the isothermal dissolution rates of the oxide films on the two alloys at various temperatures. The different dissolution temperature ranges (from 573 to 723 K for the α-Zr(1%Nb) alloy and from 448 to 548 K for the β-Zr(20%Nb) alloy) also indicate the large difference in dissolution rates between these two surfaces. Figs. 6 and 7 show the data of Figs. 4 and 5 plotted against (time)$^{1/2}$ as the horizontal axis, and the amount of oxygen *dissolved from* the oxide as the vertical axis. The excellent linear relationships shown in Figs. 6 and 7, indicate that the dissolution rates follow a parabolic law, and hence the following equation can be employed to describe the dissolution rate:

$$M(t) = Ft^{0.5}, \tag{2}$$

where $M(t)$ is the number of oxygen atoms in the oxide which have dissolved into the bulk, t is the experimental time, in s, and the F are slopes of the fits in Figs. 6 and 7 for each temperature. Since F is related to the rate of dissolution, we named it the 'dissolution factor'.

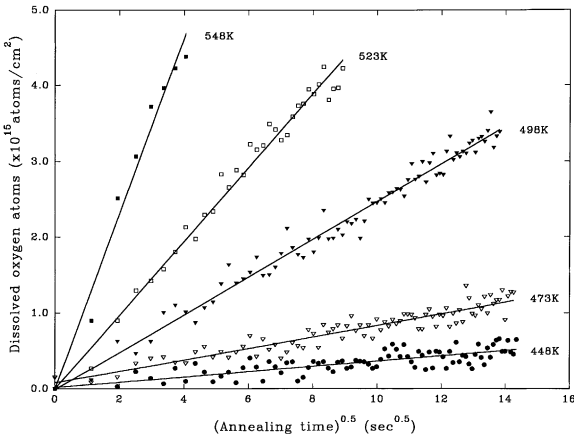

Fig. 7. The linear relationship between the amount of oxygen dissolved from the oxide film into the bulk β-(Zr–20%Nb) alloy and (annealing time)$^{1/2}$ at various temperatures.

Table 2

	Dissolution temperature (°C)	The estimated time required to dissolve 1 μm oxide (years)
The estimated time required to dissolve 1 μm oxide (years) on α-Zr(1%Nb) alloy surface		
	300	182.7
	350	53.7
	375	12.2
	400	3.9
	425	1.42
	450	0.51
The estimated time required to dissolve 1 μm oxide (years) on β-Zr(20%Nb) alloy surface		
	175	335.6
	200	73.1
	225	6.92
	250	2.15
	275	0.31

It has been found previously that dissolution of oxide on pure α-Zr followed the parabolic law indicating that oxygen diffusion from the oxide into the metal is the rate controlling step [8]. The parabolic law should therefore also be valid for dissolution of thick oxide films, because in the simplest model, oxygen diffusion into the underlying metal or alloy should not be affected by the thickness or other properties of the *oxide* film. Of course we recognize that the microstructure of the film could affect the dissolution rate, but it is likely that under the relatively low temperatures in this work that transport of the oxygen away from the oxide–alloy interface by diffusion is the rate limiting step. By using Eq. (2) and the dissolution factors, we can estimate the time required for complete dissolution of a thick oxide film. These estimates are achieved by integration of the amount dissolved until the oxygen concentration at the alloy *surface* is only a few percent of its original value in the oxide and the intensity of the $(MNV)_o$ tends to zero. Values shown for a 1-μm oxide film in Table 2 demonstrate that the time needed to dissolve a 1-μm thick oxide film on the α-Zr(1%Nb) alloy surface at 573 K is more than 500 times longer than on the β-Zr(20%Nb) alloy surface at 548 K.

The importance of this result is that in vacuum, a 1-μm thick oxide film will be stable essentially indefinitely on the α-Zr(1%Nb) alloy surface at 573 K, while the oxide film on the β-phase alloy would be completely dissolved in less than four months even at 548 K. In reactor operation, the oxidizing environment will continually regrow the oxide, but this process will have to be more rapid on the β-phase. In a real, mixed phase alloy, in which oxide exists on grains, the situation is much more complex, as oxygen dissolution/diffusion might have to occur across α–β phase boundaries. The present results clearly indicate however that the oxide films are less stable on the β-phase and that β-phase 'stringers' could well act as fast dissolution pathways. An unsolved issue is how the oxidizing species are transported to the alloy–oxide interface which is believed to be the location of the dense oxide barrier layer that prevents hydrogen ingress. Clearly if oxygen atoms are continually dissolving at this interface, this could produce a region of sub-stoichiometry that could be reactive and more 'transparent' to hydrogen permeation. For oxide regrowth, the transport of oxygen and/or water or oxygen ions could be the rate limiting step, the rate depending strongly upon the microstructure of the entire oxide layer. Since the deuterium that enters the alloy originates from water dissociation, the occurrence of more rapid dissolution at the β-phase boundaries could also mean that these are probably the locations of most of the hydrogen ingress. We also know that hydrogen diffusion is much more rapid in the β-phase alloy.

3.3. Diffusion coefficients deduced from the oxide dissolution rates

Fig. 8 is a schematic of the oxide dissolution process. Because the dissolution of oxide is controlled by diffusion of oxygen into the bulk [8], from Fick's law, the distribution of oxygen in the bulk will be

$$-D\,\mathrm{d}c/\mathrm{d}x = C(x,t) = C_s\{1 - \mathrm{erf}[x/2(Dt)^{0.5}]\}, \qquad (3)$$

where C_s is the dissolved oxygen concentration right at the metal–oxide interface (which is the oxygen solubility limit), D is the diffusion coefficient of oxygen, (assuming D is independent of the dissolved oxygen concentration), and the origin of x is always taken at the interface. The flux of oxygen atoms can then be expressed by

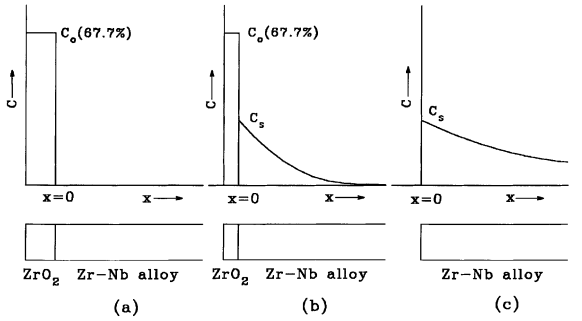

Fig. 8. Schematic of the dissolution process of a Zr oxide film.

$$J(x,t) = C_s(D/\pi t)^{0.5} \exp(-x^2/4Dt). \quad (4)$$

The amount of oxygen dissolved from the oxide into the bulk is given by

$$M(t) = 2C_s(Dt/\pi)^{0.5}. \quad (5)$$

The diffusion coefficient can be obtained from a plot of $M(t)$ versus $t^{0.5}$ if C_s is known. The value of C_s can be obtained by sputtering the oxide-covered sample and determining the O-concentration at the point at which the oxide film has just been removed (intensity of $Zr(MNV)_o = 0$). Alternatively, C_s could be obtained from the O-concentration remaining after the oxide covered sample was heated to the point where the oxide had just completely dissolved. The results from both methods are very consistent: 29% for α-Zr(1%Nb) alloy and 10% for β-Zr(20%Nb) alloy, which is also consistent with saturation concentration of oxygen in Zr indicated by the phase diagram [13].

Table 3

Temperature (K)	Diffusion coefficients ($\times 10^{-16}$ cm^2 s^{-1})
Oxygen diffusion coefficients in the α-Zr (1%Nb) alloy	
573	0.0117
623	0.359
648	1.63
673	5.45
698	14.7
723	41.3
Oxygen diffusion coefficients in the β-Zr (20%Nb) alloy	
448	0.0411
473	0.297
498	3.14
523	12.0
548	68.7

The diffusion coefficients in the α-Zr(1%Nb) and β-Zr(20%Nb) alloys determined at various temperatures by the above methods, are listed in Table 3 and shown in Fig. 9. The diffusion equations deduced from these data are

$0.172 \exp(-187.47\ \text{kJ/RT})$ for the α-Zr(1%Nb) alloy,

$0.69 \exp(-149.45\ \text{kJ/RT})$ for the β-Zr(20%Nb) alloy.

Fig. 9 compares the diffusion data from the present work with previously published work [14,15]. It can be seen in Fig. 9 that both the diffusion activation energies and the pre-exponential factors are very similar for the α-Zr(1%Nb) alloy obtained in this work and for α-Zr

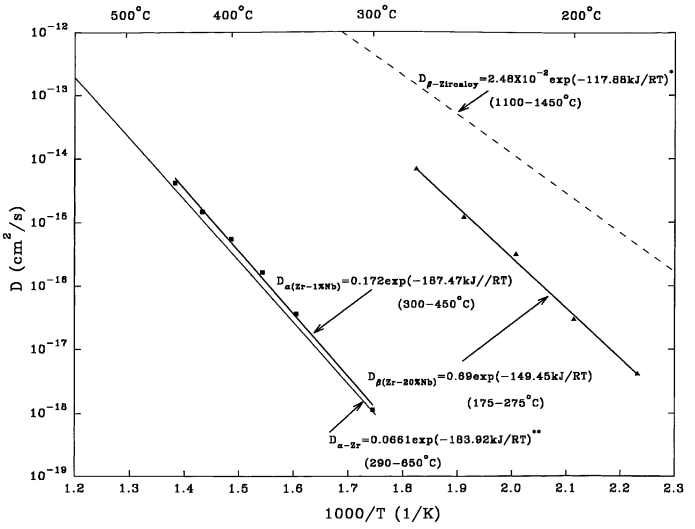

Fig. 9. Comparison of diffusion coefficients obtained from this work with the literature results. (* is extrapolated from results in Ref. [14] and ** from Ref. [15]).

measured previously [14]. The oxygen diffusion coefficient in the β-Zr(20%Nb) alloy is higher than that in α-Zr(1%Nb) alloy by more than four orders of magnitude, if the linear relationship in the plot can be extended to lower and higher temperatures.

It has been known for some time that oxygen diffusion is much more rapid in body centered cubic β-Zr or β-zircaloy than in hexagonal α-Zr or α-zircaloy [14,15]. A similar result has been obtained in the present work, indicating much faster diffusion of oxygen in β-Zr(20%Nb) alloy than in the α-Zr(1%Nb) alloy. As mentioned above, the oxygen diffusion coefficient in α-Zr(1%Nb) alloy obtained in this work is in good agreement with those for α-Zr obtained by traditional methods [14]. However there is a discrepancy between the diffusion data (pre-exponential factor and diffusion activation energy) in the β-Zr(20%Nb) alloy in the present work and literature values for β-Zr or β-zircaloy-4. (Fig. 9). This discrepancy may be attributed largely to the difference in the temperature ranges over which the diffusion coefficients were measured. The data in the literature for β-alloys were obtained at 1173 to 1373 K where the microstructure is a stable β-phase. The sample of β-Zr(20%Nb) alloy used in the present work was annealed in the β-phase region (1123 K) and then quenched rapidly to room temperature. The dissolution data were then acquired by rapid temperature jump-and-hold methods. Although the single β-phase still remained after quenching, this β-phase was supersaturated with niobium and had thus become metastable. This metastable β-phase will transform to a β-Zr phase enriched in niobium, the ω-Zr phase, α-Zr phase and the β-Nb phase. The time required to initiate these transformations at the isothermal annealing temperatures used in this work (448–623 K) is more than 10 h; this is much longer than the time spent for the dissolution (and diffusion) measurements in this work (Fig. 5). However, the 20%Nb supersaturation will, we believe affect the diffusion of oxygen and this might be the cause of the discrepancy with the diffusion data for the stable β-Zr phase.

There is another consequence of the much faster oxygen diffusion in the β-Zr(20%Nb) alloy. In another experiment (not shown in this paper) the initial apparent *oxide* growth rate on this phase at 523 K was about five times slower than on α-Zr(1%Nb) alloy at the low oxygen pressures used in this work. This occurs because the oxygen concentration in the AES sampling depth is maintained at a lower value by rapid diffusion into the bulk, thus delaying the time at which the oxygen concentration reaches the value necessary for oxide nucleation.

4. Summary

The oxide dissolution rates on β-Zr(20%Nb) and α-Zr(1%Nb) alloys have been measured by AES at various temperatures. The results indicated that oxide films on the β-Zr(20%Nb) alloy dissolve much more rapidly into the bulk alloy than is the case for the α-Zr(1%Nb) alloy. The oxygen diffusion coefficients in both the β-Zr(20%Nb) and α-Zr(1%Nb) alloys were deduced from the oxide dissolution kinetics.

References

[1] R.L. Tapping, T.S. Gendron, RC-101 Chalk River Laboratories COG-88-136, December 1988.
[2] V.F. Urbanic, Chalk River Nuclear Laboratories CRNL-2950, OH DND GEN 85431, October 1986.
[3] P.C. Lichtenberger, N. Ramasubramanian, B.D. Warr, R.L. Tapping, V.F. Urbanic, COG-91-277, February, 1992.
[4] P. Prieto, L. Galan, J.M. Sanz, F. Rueda, Surf. Interf. Anal. 16 (1990) 535.
[5] C.-S. Zhang, B. Li, P.R. Norton, Surf. Sci. 338 (1995) 157.
[6] C.-S. Zhang, B.J. Flinn, I.V. Michell, P.R. Norton, Surf. Sci. 245 (1991) 373.
[7] B.A. Cheadle, The Physical Metallurgy of Zirconium Alloy, CRNL-120g, Metallurgical Engineering Branch, Chalk River Nuclear Laboratories, Chalk River, Ontario, October 1974.
[8] C.-S. Zhang, B. Li, P.R. Norton, Surf. Sci. 313 (1994) 308.
[9] I.V. Mitchell, G.R. Massoumi, W.N. Lennard, S.Y. Tong, P.E.A. Alkemade, K. Griffiths, S.J. Bushby, P.R. Norton, Nucl. Instrum. Methods B 45 (1990) 107.
[10] C.-S. Zhang, B.J. Flinn, P.R. Norton, Surf. Sci. 264 (1992) 1.
[11] G.A. Somojai, Chemistry in Two Dimensions, Cornell University, Ithaca, NY, 1981.
[12] M.P. Seah, W.A. Dench, Surf. Interface Anal. 1 (1979) 2.
[13] T.B. Massalski et al., in: Binary Alloy Phase Diagrams, vol. 2, American Society for Metals, Metals Park, OH, 1986, p. 1800.
[14] I.G. Ritchie, A. Atrens, J. Nucl. Mater. 50 (1974) 247.
[15] P.A. Perkins, J. Nucl. Mater. 68 (1977) 148.